Biophysical Journal Volume 96 March 2009 2204–2215

Structure of Ceramide-1-Phosphate at the Air-Water Solution Interface in the Absence and Presence of Ca^{2+}

Edgar E. Kooijman,[†*] David Vaknin,[‡] Wei Bu,[‡] Leela Joshi,[§] Shin-Woong Kang,[§] Arne Gericke,[¶]
Elizabeth K. Mann,[§] and Satyendra Kumar[§‖]

[†]Department of Biological Sciences, Kent State University, Kent, Ohio 44242; [‡]Ames Laboratory and Department of Physics and Astronomy, Iowa State University, Ames, Iowa 50011; [§]Physics Department, Kent State University, Kent, Ohio 44242; [¶]Chemistry Department, Kent State University, Kent, Ohio 44242; and [‖]Division of Materials Research, National Science Foundation, Arlington, Virginia 22203

ABSTRACT Ceramide-1-phosphate, the phosphorylated form of ceramide, gained attention recently due to its diverse intracellular roles, in particular in inflammation mediated by $cPLA_2\alpha$. However, surprisingly little is known about the physical chemical properties of this lipid and its potential impact on physiological function. For example, the presence of Ca^{2+} is indispensable for the interaction of Cer-1-P with the C2 domain of $cPLA_2\alpha$. We report on the structure and morphology of Cer-1-P in monomolecular layers at the air/water solution interface in the absence and presence of Ca^{2+} using diverse biophysical techniques, including synchrotron x-ray reflectivity and grazing angle diffraction, to gain insight into the role and function of Cer-1-P in biomembranes. We show that relatively small changes in pH and the presence of monovalent cations dramatically affect the behavior of Cer-1-P. On pure water Cer-1-P forms a solid monolayer despite the negative charge of the phosphomonoester headgroup. In contrast, pH 7.2 buffer yields a considerably less solid-like monolayer, indicating that charge-charge repulsion becomes important at higher pH. Calcium was found to bind strongly to the headgroup of Cer-1-P even in the presence of a 100-fold larger Na^+ concentration. Analysis of the x-ray reflectivity data allowed us to estimate how much Ca^{2+} is bound to the headgroup, ~0.5 Ca^{2+} and ~1.0 Ca^{2+} ions per Cer-1-P molecule for the water and buffer subphase respectively. These results can be qualitatively understood based on the molecular structure of Cer-1-P and the electrostatic/hydrogen-bond interactions of its phosphomonoester headgroup. Biological implications of our results are also discussed.

INTRODUCTION

Sphingolipids are an important component of biological membranes, in particular the plasma membrane of cells. These lipids are mainly synthesized in the Golgi complex and their concentrations vary among the different intracellular compartments (1–3). Sphingolipids consist of the amino-alcohol sphingosine with or without an amine-linked fatty acid and various alcohol bases and/or carbohydrate groups attached to the C-1 hydroxyl group. Fig. 1 shows the chemical structures of sphingomyelin (SM), ceramide (Cer) and ceramide-1-phosphate (Cer-1-P), the subject of this study. The amino-alcohol group sets them apart from the more common glycerol based (phospho)-lipids. Perhaps the most important of these distinguishing properties is the possibility for the amine and the C-3 hydroxyl group to form an intermolecular hydrogen bond between neighboring sphingolipids (4–6). These strong intermolecular interactions coupled with the saturated/trans unsaturated nature of the hydrocarbon chains results in the formation of rigid, gel-type bilayer membranes of the most common sphingolipid, SM (7). These interactions also play an important role in the Cers that are present in the stratum corneum, where highly ordered crystalline and gel phases have been observed (7–9). In plasma membranes, the strong mutual interaction between SM lipids is mediated by the presence of cholesterol, which leads to the formation of liquid-ordered domains, also termed lipid rafts (10). In contrast to SM, Cer has not been found to form a liquid-ordered phase with cholesterol and instead Cer forms together with SM a gel phase within an otherwise liquid-ordered SM/cholesterol domain (11,12).

Aside from its rich functionality (phosphomonoester, free hydroxyl group, and amine linked acyl chain), it was realized recently that Cer-1-P has important intracellular functions (13). Therefore, it is not only important from a physical chemistry point of view to compare Cer-1-P with the other more common sphingolipids such as SM and Cer but to also investigate Cer-1-P monolayer behavior to relate its interfacial properties to its potential role in biological membranes (14,15).

Cer-1-P fulfills an important role as a novel second messenger and is involved in (intra)cellular processes as diverse as phagocytosis (16), potassium channel function (17), inflammatory responses (18–21), and cell survival and tumorigenesis (13,22–24). The exact mechanism of Cer-1-P action in these processes is not yet clear, although two alternate, and not mutually exclusive, possibilities are likely. Cer-1-P may function by direct interaction through the activation/recruitment of effector proteins such as $cPLA_2\alpha$ (19,25), and/or indirectly by affecting membrane fluidity, curvature and electrostatics (26–28). In the case of $cPLA_2\alpha$, the activation of the enzyme is calcium dependent, and due to its highly negatively charged phosphomonoester

---

Submitted May 6, 2008, and accepted for publication November 18, 2008.

*Correspondence: e.e.kooijman@gmail.com

Editor: Lukas K. Tamm.

© 2009 by the Biophysical Society

0006-3495/09/03/2204/12 $2.00

doi: 10.1016/j.bpj.2008.11.062

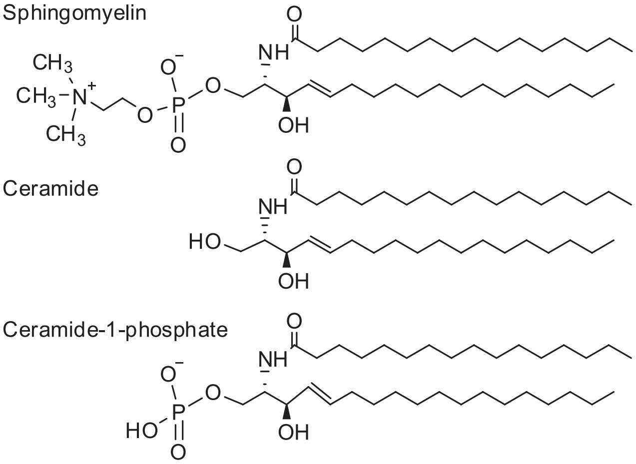

FIGURE 1 Chemical structures of sphingomyelin, ceramide, and ceramide-1-phosphate carrying a C16 saturated fatty acid (palmitic acid).

headgroup (28), divalent cations likely play an important role in the phase properties of Cer-1-P.

The phase behavior and monolayer properties of many sphingolipids have been investigated in detail before (4–6, 29–31). Ceramide forms solid monolayers that are characterized by an asymmetry in the hydrocarbon chains. Similar behavior has been found for SM. Cer-1-P differs from SM and Cer by differences in its headgroup. Despite its physiological importance, no study is currently available detailing the phase behavior and structural properties of Cer-1-P model membrane systems in the presence and absence of Ca^{2+}.

Our goal is to determine the phase behavior and structural properties of Cer-1-P in monomolecular films at the air-liquid interface in the absence and presence of mM quantities of calcium. Using surface pressure versus molecular area isotherms, Brewster angle microscopy (BAM) and liquid surface-sensitive x-ray scattering techniques we studied the monomolecular structure at molecular length scales of Cer-1-P. These experiments were carried out on four different subphases, pure water, 1 mM $CaCl_2$, pH 7.2 buffer, and pH 7.2 buffer + 1 mM $CaCl_2$. These four subphases were chosen to allow comparison with previous data on ceramide and sphingomyelin (obtained on a pure water subphase) and to shed light on the physiological functions of Cer-1-P.

MATERIALS AND METHODS

N-hexadecanoyl-D-erythro-sphingosine-1-phosphate, NH_4^+salt (Cer-1-P), was purchased from Matreya, LLC (Pleasant Gap, PA) and used without further purification. Other chemicals used were at least 99.8% pure and purchased from Sigma (St. Louis, MO). The synthetic Cer-1-P from Matreya LLC was found to be hard to dissolve and the recommended solvent, chloroform/methanol/acetic acid, 60:15:25, is inappropriate for the formation of monomolecular layers at the air/water interface, because the use of this solvent mixture results in a partial solution of Cer-1-P into the subphase. Instead, Cer-1-P was found to dissolve readily in a solvent mixture of chloroform/methanol/0.5 N HCl, 20:9:1, which proved more suitable for monolayer preparation. Lipid stock solutions were used within 2–3 weeks after preparation. Thin layer chromatography combined with iodine staining was used regularly to check the purity and integrity of Cer-1-P (at least >99% on HPTLC plates) at various times after solubilization; no breakdown was observed during the course of our experiments (after solubilization and storage at −20°C). Lipid concentration was determined by following a phosphate determination protocol (32). All glassware was cleaned using either concentrated H_2SO_4 or a concentrated KOH (24g H_2O, 25g KOH, and 164g C_2H_5OH) solution to avoid contamination of stocks, water and buffer.

π-A isotherms

Langmuir monolayers were formed on two different Langmuir troughs. At the Advanced Photon Source (APS) of Argonne National Laboratories, the monolayers were spread in a temperature controlled (20 ± 1°C) home built Langmuir monolayer trough in a gas-tight aluminum container and surface tension was recorded using a filter-paper Wilhelmy plate. Generally ~40 μL of a 1 mM Cer-1-P stock solution was spread on the ~250 mL subphase. Compression of the monolayers occurred asymmetrically at 1.8 Å^2 per molecule per minute (Å^2 $\times$ mol^{-1} $\times$ min^{-1}). Langmuir monolayers for isotherm and BAM measurements were formed on a temperature controlled (20 ± 1°C) KSV (KSV, Helsinki, Finland) mini-trough system and surface tension was recorded using a platinum Wilhelmy plate; ~20 μL of a 1 mM Cer-1-P stock solution was spread on the ~150 mL subphase. Compression of the monolayer was symmetric at 2.0 Å^2 $\times$ mol^{-1} $\times$ min^{-1}. Four different subphases were used in the current study, i.e., pure water and pH 7.2 buffer (10 mM Tris-HCl, 150 mM NaCl, 0.2 mM EDTA) with and without 1 mM $CaCl_2$ (in the latter the EDTA was omitted). Water used in the experiments came from a Milli-Q (Millipore, Bedford, MA) (at the APS) or from a Purelab Plus UV system (Siemans, Warrendale, PA), for isotherm and BAM measurements and in both cases had a resistivity of 18.2 MΩ-cm and passed the shake test. The pH of the water subphase was found to be ~6.0 after deposition of Cer-1-P and therefore fell in the range of $5.5 < pH < 6.5$ generally accepted as the pH of pure water kept in air. The pH of the buffer subphase was not altered by the deposition of Cer-1-P and was constant at pH 7.2.

BAM

Brewster angle microscopy (33,34) was carried out on a home built BAM microscope using the standard design (33,34). Incident light at 668 nm (SDL 7470-P6), polarized in the plane of incidence, was reflected of the air/liquid interface at the Brewster angle to a biconvex lens (focal length of 10 cm) that focused the image on a CCD camera (Panasonic GP-MF602). The resolution is estimated to be ~50 μm with a field of view of 1 cm. During the experiments (compression, decompression, and gentle agitation), images were captured directly from the camera output by a frame grabber. Surface pressure measurements were recorded simultaneously using the KSV system. Video and image analyzes was carried out using Ulead VideoStudio 6SE and ImageJ by Wayne Rasband (National Institutes of Health), respectively.

X-ray scattering

X-ray studies at the gas-water (buffer) interface were conducted on the Ames Laboratory liquid surface diffractometer at the APS, beamline 6ID-B. A detailed description of the experimental set up can be found elsewhere (35). To reduce x-ray damage of the monolayer due to the formation of free radicals and ions and to reduce background scattering from air, the thermostated trough was kept under a water-saturated helium atmosphere. The trough is mounted on a motorized stage that can be translated laterally to inspect radiation damage by illuminating different parts of the monolayer. During the course of our experiments no significant radiation damage was observed as indicated by an identical reflectivity curve after several experiments. The highly monochromatic beam (16.2 keV, $\lambda = 0.765334$ Å) was selected by a downstream Si double crystal monochromator and is deflected onto the liquid surface to a desired angle of incidence with respect to the liquid surface by a second monochromator (Ge(220) crystal) located on the diffractometer. The rectangular shaped incident beam is ~80 μm by ~2 mm, and the detector (Cyberstar Scintillator NaI(Tl); FMB, Oxford, UK) aperture in reflectivity configuration is 1 × 2 mm.

X-ray reflectivity (XR) in combination with grazing incidence x-ray diffraction (GIXD) are common techniques to investigate the detailed molecular arrangements in monomolecular layers at the air-liquid interface (35,36). Specular XR experiments yield the electron density (ED) profiles across the interface and can be related to the molecular structure of the film. The electron density profile across the interface is obtained by a two-stage refinement of a slab model that best fits the measured reflectivity by the nonlinear least-squares method. The ED profile $\rho(z)$ is constructed by a sum of error functions:

$$\rho(z) = \frac{1}{2}\sum_{\mathrm{i}=1}^{\mathrm{N}+1}\mathrm{erf}\left(\frac{z-z_{\mathrm{i}}}{\sqrt{2}\sigma_{\mathrm{i}}}\right)(\rho_{\mathrm{i}}-\rho_{\mathrm{i}+1}) + \frac{\rho_1}{2} \qquad (1)$$

where $N+1$ is the number of interfaces, $(\rho_{\mathrm{i}}-\rho_{\mathrm{i}+1})$, z_{i} and σ_{i} are the change in the ED, the position, and the roughness of the ith interface, respectively, ρ_1 is the ED of the subphase (≈ 0.334 e/Å^3 for water and 1 mM CaCl$_2$, and ≈ 0.336 e/Å^3 for buffer subphases), and $\rho_{\mathrm{N}+2} \approx 0$ is the density of the gas phase. The variable parameters are ρ_{i}, z_{i}, (the thickness of the slabs associated with different parts of the molecules are denoted as $d_{\mathrm{i}} \equiv |z_{\mathrm{i}} - z_{\mathrm{i}-1}|$), and the roughness σ_{i}. The continuous ED is sliced into a histogram (several hundred slices) to compute the reflectivity by the recursive dynamical method (35,37–39). Errors for the fit parameters were determined by finding a + and − value for each of the parameters that resulted in a 50% increase in the χ^2 (measure of the goodness of the fit) of the fit.

GIXD experiments were conducted to determine the lateral organization in the film. In these experiments, the angle of the incident beam with respect to the surface, α, is fixed below the critical angle ($\alpha_{\mathrm{c}} = \lambda(\rho_{\mathrm{s}} r_0/\pi)^{1/2} = 0.0759°$, where; $r_0 = 2.82 \times 10^{-13}$ cm, and ρ_{s} is the subphase ED) for total reflection, whereas the diffracted beam is detected at a finite azimuthal in-plane angle, 2Θ, and out-of-plane angle, β (the angle of the reflected beam with respect to the surface). Rod-scans, the intensity distribution of the 2D Bragg reflections normal to the surface, were measured with a position sensitive detector (PSD-50M-ASA, MBraun, Garching, Germany) situated behind a Soller collimator (0.1° divergence). Analysis of these rod-scans in the framework of the distorted wave Born approximation (35,40) enables the determination of the average ordered chain length and tilt angle with respect to the surface normal.

The coordinate system is chosen such that Q_{z} is normal to the liquid surface, Q_{x} is parallel to the horizontal (untilted) incident x-ray beam, and Q_{y} is orthogonal to both Q_{z} and Q_{x}. The hydrocarbon chains of Cer-1-P form 2D poly crystals, giving rise to a diffraction pattern that depends on the modulus of the in-plane momentum transfer $Q_{\mathrm{xy}} = \sqrt{(Q_{\mathrm{x}}^2 + Q_{\mathrm{y}}^2)}$, and is practically independent of rotation of the sample over the z axis. The GIXD data are plotted in a 2D map of Q_{z} versus Q_{xy}.

RESULTS

π-A isotherms and Brewster angle microscopy

First we used surface pressure versus molecular area isotherms coupled with Brewster angle microscopy to characterize the thermodynamic properties and the macroscopic morphology of Cer-1-P monolayers. Representative surface pressure versus molecular area isotherms for Cer-1-P on four subphases, i.e., pure water, 1 mM CaCl$_2$, pH 7.2 buffer, and pH 7.2 buffer + 1 mM CaCl$_2$, are shown in Fig. 2 *A*. On a water subphase (Fig. 2, *solid curve*), the increase in surface pressure with decreasing area is rapid and occurs over a narrow molecular area range (~6–8 Å^2/mol). The initial increase in surface pressure exerted by the films on the different subphases is noisy with jumps on the order of 0.02 mN/m, sometimes followed by stabilization of the surface pressure and then again a jump, until finally at a smaller area (80–70 Å^2/mol) the pressure starts to increase monotonically (Fig. 2 *A*, *inset*). The rapid increase in molecular area (from ~55 to ~43 Å^2/mol, the range for all the isotherms shown) coupled to the initial ‘‘noisy’’ increase in pressure is indicative of the formation of a solid like Cer-1-P monolayer, very similar to what was found previously for ceramide (5,29).

It should be noted that the isotherms shown are representative, and a variation in the molecular area at collapse does occur within ~5–10% between experiments and different batches of Cer-1-P stock. This may be caused by the solid-like/semi-crystalline nature of the monolayer that reduces the reproducibility (due to defects between crystalline

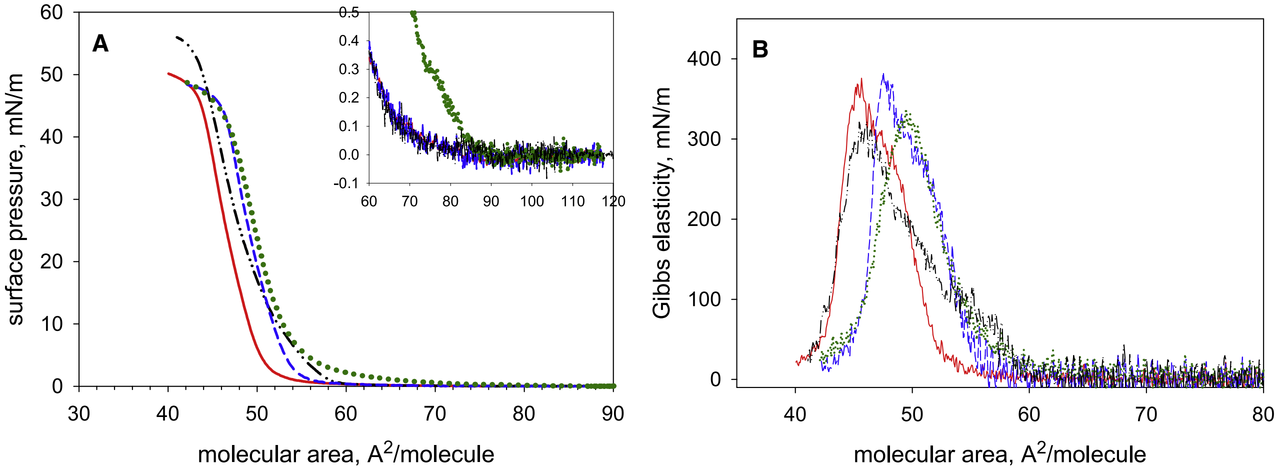

FIGURE 2 (*A*) Area versus surface pressure isotherms for ceramide-1-phosphate on four different subphases. Curves indicate representative isotherms for Cer-1-P on water (*solid*), on pH 7.2 buffer (*long dash-dot-dot*), on 1 mM Ca^{2+} (*short dash*), and on buffer pH 7.2 + 1 mM Ca^{2+} (*dotted*). Right-hand inset shows a blow up of the initial increase in surface pressure. (*B*) Gibbs elasticity in mN/m calculated for the isotherms shown in *A*. Note that the area for the peak elasticity varies between experiments on the same subphase by ~10%, so that the apparent difference in this area is not significant.

domains), and due to small errors in determining the actual concentration of our lipid stocks using the phosphate determination (error estimated to be $<\sim 2\%$). However the slopes of the isotherms are highly reproducible.

Brewster angle microscopy of a Cer-1-P monolayer on water, as shown in Fig. 3, supports the view of the formation of a highly crystalline monolayer. After spreading from organic solvent at a molecular area of 117 Å^2/mol, many sharp edged domains are visible (Fig. 3 *A*). On compression, these domains come closer and fuse to form ultimately a uniform (on the BAM resolution length-scale) monolayer (Fig. 3, *B* and *C* respectively). It should be noted that the speckled nature of this and the other images is due to inhomogeneities in the laser intensity profile and not due to any type of structure in the film. After decompression to 117 Å^2/mol the reflected intensity from the monolayer does not change significantly, except for the appearance of small irregular ''cracks'' as indicated by the two arrows in Fig. 3 *D*. At this point the monolayer was gently agitated by a weak stream of air. This resulted in a breaking of what appears like a very crystalline monolayer, reminiscent of the breaking of a sheet of ice on water. This is clearly visible by the three large sheets of monolayer present after agitation. After this breakage and subsequent recompression, these sheets fused to form again a continuous layer, indicating that the breaking is reversible on the BAM length scale (data not shown; see Movie S1 in the Supporting Material). Collapse of the Cer-1-P monolayer on water occurs by the buckling (folding onto itself) of the monolayer as evidenced by the stripe pattern as shown in Fig. S1, *a* and *b*. This buckling is irreversible, indicated by a large area hysteresis on subsequent de- and recompression of the monolayer. That is, subsequent isotherms trace the initial one except at lower molecular area.

Compared to the isotherm for Cer-1-P on pure water, the increase in surface pressure for Cer-1-P on pH 7.2 buffer (Fig. 2 *A*) is considerably more gradual. Also the collapse pressure for Cer-1-P on the pH 7.2 buffer subphase is ~5–10 mN/m higher. To quantitatively compare the behavior of Cer-1-P on water, buffer, and the calcium containing subphases (discussed below), we calculated the Gibbs elasticity ($E_G = -A(d\pi/dA)$) as a function of molecular area of the films. The results in Fig. 2 *B* show that Cer-1-P indeed forms very stiff solid-like monolayers as indicated by the large Gibbs elasticity. However, the Gibbs elasticity for the monolayer on buffer is consistently lower by ~70 mN/m than that of the monolayer on water, i.e., the slopes of the isotherms nicely overlap. An indication of this overlap is the fact that the deviation in the E_{Gmax} for the Cer-1-P monolayer on pure water (three independent isotherms) is $<\sim 5$ mN/m and clearly falls within the noise of the E_G versus area curves.

After spreading at 117 Å^2/mol the Cer-1-P monolayer on pH 7.2 buffer looks more homogeneous compared to the monolayer on water, even though there are still defects present that suggest a ''solid'' like monolayer (Fig. 3 *E*). At 80 Å^2/mol most of these defects are not visible, with an intact monolayer at 48.3 Å^2/mol (Fig. 3, *F* and *G*). On decompression to 117 Å^2/mol, the monolayer remains visible in the field of view of the CCD camera, but with a considerably lower intensity when compared to the

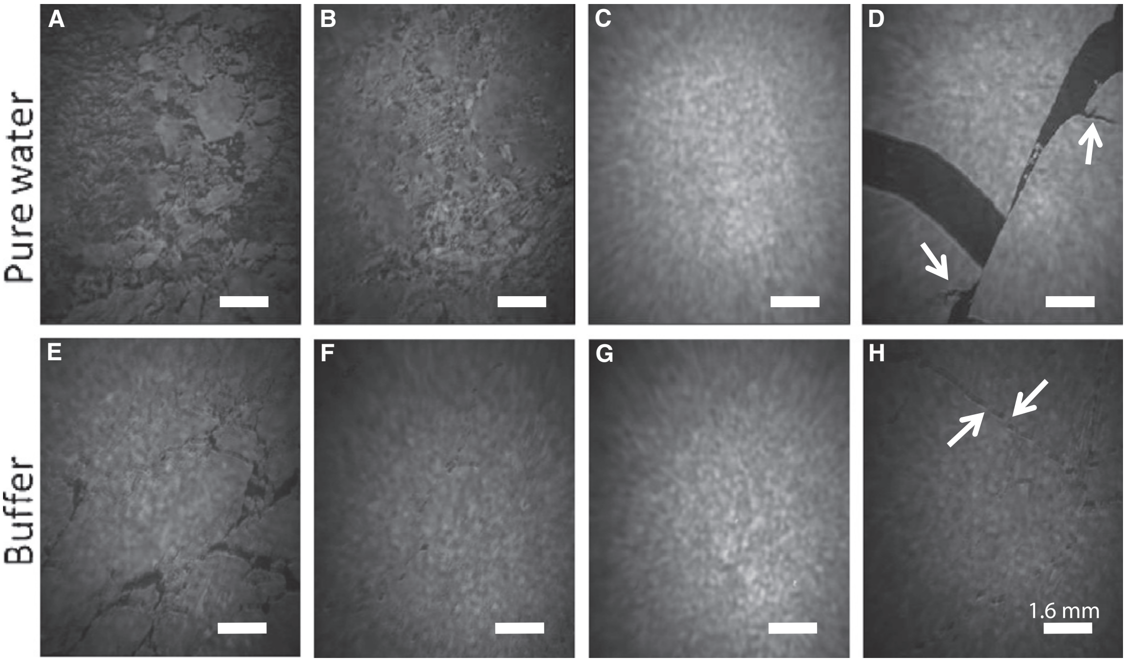

FIGURE 3 Brewster angle microscopy of ceramide-1-phosphate on a (*A*–*D*) H_2O subphase and a (*E*–*H*) buffer subphase. BAM images correspond to the following molecular areas for cer-1-p: (*A* and *E*) 117 Å^2/mol ~4 min after depositing the monolayer; (*b* and *f*) 80 Å^2/mol; (*C* and *G*) 48.3 Å^2/mol; (*D* and *H*) after decompression to 117 Å^2/mol and gentle agitation of the monolayer by a stream of air.

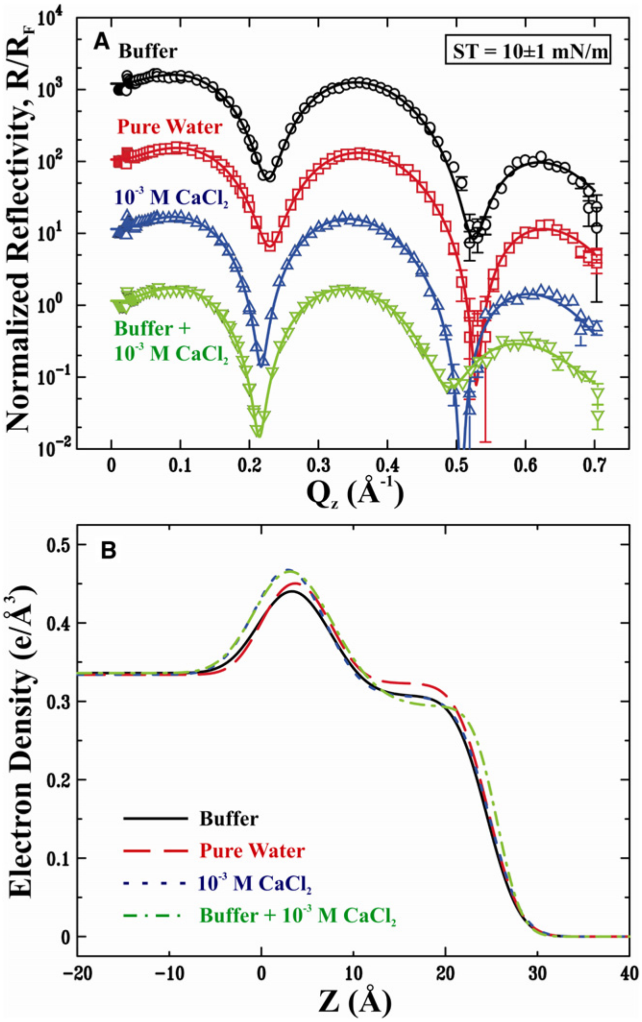

FIGURE 4 (*A*) Normalized reflectivity's of ceramide-1-phosphate on four different subphases as indicated at a surface pressure of 10 ± 1 mN/m. Solid lines are best-fit curves, as discussed in the text. (*B*) Electron densities used for creating the corresponding reflectivity curves in *A*.

monolayer on pure water (Fig. S2). This decrease in intensity indicates a decrease in the reflectivity of the monolayer due to a thinner or more tenuous monolayer. Unlike in the case of the water subphase the Cer-1-P molecules on the buffer subphase appear to respread, resulting in the occupation of a larger molecular area. On water, after decompression the solid-like slab of Cer-1-P remains essentially immobile in the center of the trough. Again small ''defects'' are present after decompression on the buffer subphase, but these are more uniform in shape than the jagged edges in the monolayer on water (data not shown). Air agitation of the monolayer produces similar cracks as those found for the monolayer on water with the major difference that these appear to bleed into each other and partially fuse (Movie S2). Several such areas that are filling in again are indicated by an arrow in Fig. 3 *H*. The shape of subsequent isotherms is identical to the original one, as in the case of the water subphase, but recompression isotherms trace the original isotherm at smaller molecular areas, indicating that a fraction of Cer-1-P is lost from the original monolayer. This may be due to a partial coating of Cer-1-P on the platinum plate, barriers, or edges of the trough.

We conclude that the collapse behavior of the Cer-1-P monolayer on buffer is very different from that on water as shown in Fig. S1, *c* and *d*. That is, no clear 3D structures appear on collapse of the Cer-1-P monolayer on buffer and the area hysteresis (see above) is also smaller than for the monolayer on pure water. This differential response clearly reflects the sensitivity of the phosphomonoester headgroup of Cer-1-P to pH and ionic conditions of the subphase.

Addition of 1 mM Ca^{2+} to the water or buffer subphase does not seem to significantly alter the isotherms in comparison to their Ca^{2+}-free counterparts. The Gibbs elasticity is only marginally larger in the presence of Ca^{2+} (Fig. 2 *B*), potentially due to the very large values of the elasticity in the situation without Ca^{2+}. The largest difference appears to occur for the pH 7.2 buffer + 1 mM Ca^{2+} subphase, where the lift off (the point where surface pressure increases) appears to occur at larger molecular areas. Thus in general the initial increase in surface pressure seems to occur at larger areas (but keeping in mind the area variation between experiments) and the increase in pressure is slightly steeper, i.e., E_G is consistently higher, than for the monolayer on buffer (Fig. 2, *A* and *B*).

There are two main messages that can be deduced from the isotherms and the BAM microscopy experiments. First, at high pressure the monolayers form a highly condensed phase, irrespective of subphase composition, as indicated by the high elasticity of the films. Second is the striking effect of the physiologically relevant buffer subphase on the behavior of Cer-1-P, imparting a more fluid-like nature to the film. This enhanced ''fluidity'' indicates a strong response of the phosphomonoester headgroup of Cer-1-P to changes in pH and ionic strength of the surrounding medium.

X-ray reflectivity

Specular reflectivity was measured at several points along the isotherm (at different pressures, i.e., molecular area).

TABLE 1 Parameters that produce the best fit calculated reflectivity to the experimental data shown in Fig. 4 *A*

Subphase	Pure water	1 mM CaCl$_2$	Buffer	Buffer + 1 mM CaCl$_2$
σ_0 (Å)	2.4 ± 1.0	3.2 ± 0.9	$2.9 \pm {}^{1.1}_{1.5}$	$3.2 \pm {}^{0.8}_{1.0}$
d_{head1} (Å)	$7.7 \pm {}^{1.3}_{2.6}$	$6.1 \pm {}^{2.2}_{2.7}$	$7.3 \pm {}^{2.2}_{3.5}$	$6.6 \pm {}^{3.8}_{2.1}$
ρ_{head1} (e/Å^3)	$0.47 \pm {}^{0.07}_{0.03}$	$0.55 \pm {}^{0.05}_{0.07}$	$0.48 \pm {}^{0.06}_{0.04}$	$0.56 \pm {}^{0.14}_{0.07}$
σ_1 (Å)	$2.6 \pm {}^{0.9}_{1.0}$	$3.5 \pm {}^{0.8}_{1.0}$	$3.3 \pm {}^{1.1}_{1.8}$	4.5 ± 1.3
d_{chain} (Å)	$17.0 \pm {}^{1.3}_{0.7}$	$18.6 \pm {}^{1.5}_{1.0}$	$17.2 \pm {}^{1.4}_{1.2}$	$19.0 \pm {}^{2.3}_{1.6}$
ρ_{chain} (e/Å^3)	$0.323 \pm {}^{0.010}_{0.015}$	$0.306 \pm {}^{0.020}_{0.016}$	$0.31 \pm {}^{0.03}_{0.01}$	$0.293 \pm {}^{0.016}_{0.014}$
σ_3 (Å)	$2.75 \pm {}^{0.30}_{0.16}$	$2.8 \pm {}^{0.3}_{0.2}$	$2.8 \pm {}^{0.6}_{0.2}$	2.1 ± 0.2

These parameters are also used to calculate the respective EDs shown in Fig. 4 *B*.

Fig. 4 *A* shows four reflectivity curves for Cer-1-P at 10 ± 1 mN/m on the four different subphases investigated, i.e., buffer, pure water, 1 mM $CaCl_2$ and buffer + 1 mM $CaCl_2$ as indicated. This pressure was chosen because it shows the general trends observed for all the pressures investigated. The fit parameters, the electron density, thickness, and roughness of the slabs for the four different subphases plus the respective errors are listed in Table 1 and the calculated ED profiles are shown in Fig. 4 *B*. These ED profiles, although similar, clearly exhibit important differences.

The electron density in the headgroup region of Cer-1-P is significantly increased by the addition of $CaCl_2$ to the subphases, indicating that Ca^{2+} binds to the negatively charged headgroup of Cer-1-P. The ED in the headgroup of Cer-1-P is not significantly different between the pure water and buffer subphases, indicating that Na^+ does not significantly bind to the phosphomonoester of Cer-1-P at these concentrations (150 mM). In the case of the buffer +1 mM Ca^{2+} subphase, the ED profile does not significantly deviate from that of the 1 mM nonbuffered subphase, except for a slightly larger electron density (indicated by the broader ED profile of the headgroup). Also the electron density for the hydrocarbon region of Cer-1-P on the pure water subphase is slightly larger at 10 mN/m than for the other subphases, consistent with the isotherms shown in Fig. 2, in that the increase in pressure occurs at slightly lower molecular area (higher molecular density, and thus ED). Data recorded at 30 ± 2 mN/m showed identical trends (reflectivity data not shown).

At this stage of the analysis we relate the electron densities to the chemical structure of Cer-1-P. This analysis, based on volume constraints, allows us to determine an average molecular structure of Cer-1-P on the individual subphases, and estimate the number of bound water molecules and ions in the headgroup region of Cer-1-P. The electron density for the hydrocarbon slab is given by,

$$\rho_{\text{tail}} = N_{\text{tail}}/d_{\text{tail}}A, \tag{2}$$

where $N_{\text{tail}} = 240$ is the total number of electrons in the hydrocarbon region of Cer-1-P starting at the double bond of the sphingosine backbone (Fig. 1). Given ρ_{tail} and d_{tail} from the fits we can now calculate the molecular area, A, for each of the different subphases; listed in Table 2 together with the uncertainties based on the reflectivity parameter errors (Table 1). Similarly we can relate the electron density in the headgroup region to the number of electrons in the headgroup, taking into account water molecules (and ions) in this region,

TABLE 2 Molecular areas, bound number of water molecules, and ions (Ca^{2+} and Na^+) calculated from the reflectivity data shown in Table 1*

Subphase	Pure water	1 mM $CaCl_2$	Buffer	Buffer + 1 mM $CaCl_2$
A_m (Å^2)	$43.7 \pm^{2.7}_{3.0}$	$42.2 \pm^{3.7}_{3.8}$	$45.0 \pm^{4.6}_{4.1}$	$43.1 \pm^{4.4}_{4.5}$
V_{head} (Å^3)	171 ± 10	171 ± 10	171 ± 10	171 ± 10
N_{H_2O}	$5.4 \pm^{2.7}_{4.4}$	$2.8 \pm^{5.2}_{2.8}$	5.2 ± 4.7	$3.6 \pm^{7.3}_{3.6}$
$N_{Ca^{2+}}$	n/a	$0.58 \pm^{0.13}_{0.12}$	n/a	$1.10 \pm^{0.18}_{0.08}$
N_{Na^+}	n/a	n/a	$0.26 \pm^{0}_{0.26}$	n/a

Only the error in reflectivity data has been taken into account.

$$\rho_{\text{head}} = (N_{H_2O}Z_{H_2O} + Z_{\text{head}})/d_{\text{head}}A, \tag{3}$$

where N_{H_2O} is the number of water molecules associated with the headgroup, $Z_{H_2O} = 10$ is the number of electrons in a water molecule, $Z_{\text{head}} = 103$ the number of electrons in the headgroup, and ρ_{head} and d_{head} are given by the XR analysis (Table 1). By applying the following volume constraint,

$$d_{\text{head}}A = N_{H_2O}V_{H_2O} + V_{\text{head}}, \tag{4}$$

where $V_{H_2O} \approx 30$ Å^3 is the volume of a water molecule, and V_{head} is the volume of the headgroup, and by using Eq. 3 we can find the molecular volume of the headgroup of Cer-1-P and the number of water molecules bound to the headgroup on the water subphase.

To account for the presence of ions, Eqs. 3 and 4 require an additional term. In Eq. 3 the additional term for the buffer subphase is $N_{Na^+}Z_{Na^+}$, where $Z_{Na^+} = 10$ is the number of electrons in a sodium ion, and for the Ca^{2+} containing subphases $N_{Ca^{2+}}Z_{Ca^{2+}}$, where $Z_{Ca^{2+}} = 18$ the number of electrons in a calcium ion. Similarly Eq. 4 is modified to include the term; $N_{Na^+}V_{Na^+}$, where $V_{Na^+} = 4.445$ Å^3 or $N_{Ca^{2+}}V_{Ca^{2+}}$, where $V_{Ca^{2+}} = 4.064$ Å^3 (ionic volumes were calculated from ionic radii found in standard tables (41)). In the case of the buffer + Ca^{2+} subphase it is assumed that there are no Na^+ ions present in the headgroup region. This is a reasonable assumption because the divalent Ca^{2+} ion clearly has a larger affinity for the interface than the monovalent sodium ion (39,42–44). This is also clear when we compare the headgroup electron density in Table 1 for the buffer and pure water subphase with those containing 1 mM Ca^{2+}. The Ca^{2+} containing subphases clearly result in a higher electron density in the headgroup than those that do not, even though the sodium concentration is at least 100 times larger than that of calcium. From Eqs. 2–4 we can now calculate the number of water molecules and ions in the headgroup region of Cer-1-P on the four different subphases. The results are given in Table 2. From our analysis it is clear that water and buffer subphases are associated with a different amount of Ca^{2+} ion bound to the headgroup of Cer-1-P (0.5 for water and 1.0 for buffer). In fact, these numbers give a rough estimate of the degree of ionization of the Cer-1-P headgroup on these two different subphases.

In this analysis we have parsed the (C16) Cer-1-P molecule into different regions as indicated by the number of electrons in the tail (240) and headgroup (103). This parsing is made as an educated guess based on the chemical structure of (C16) Cer-1-P and assumes that the headgroup of Cer-1-P includes the phosphate, C1 through C3 (plus hydroxyl group) carbons of the sphingosine backbone including the amine group and the carbonyl group of the attached fatty acid (see Fig. 1). This division results in a headgroup volume of 171 ± 10 Å^3 (Table 2), which is in general agreement with the volume estimated from x-ray diffraction data of L$_\alpha$ phase phosphatidylcholine lipids ~230 Å^3 (Table 2, (45)). The larger value obtained from the volumes recorded by Nagle et al. (45) is likely due to a difference in phase state, with the x-ray diffraction data recorded in the fluid phase whereas our data are recorded in a crystalline phase.

Changing the number of electrons in the acyl chain and headgroup slabs clearly affects the number of bound waters and ions found from the analysis above. Because the exact location of the chain/headgroup interface is unknown, we carried out the above calculations using slightly different numbers of electrons in each of the slabs, by including or excluding 6 electrons (corresponding to one carbon atom) in the tail/headgroup region of the molecule. This procedure is included in the evaluation of the error bars shown in Table 3 (i.e., combined reflectivity and estimated parsing errors).

Reflectivity was also recorded at low molecular area where the monolayer does not yet exert a measurable surface pressure, as shown in Fig. 5. The solid lines represent fits to the data as described above but they cannot be described simply by a slab model (solid lines are meant as a guide to the eye). This is because not the entire area of the trough is covered as it is evident from the Brewster angle microscopy images shown in Fig. 3. However, it is clear from these data that Cer-1-P on buffer at pH 7.2 deviates in behavior from that of the other subphases investigated. No interference pattern (no minima) is observed over the entire Q_z region probed, indicating a thin slab of electron density (~10 Å) most consistent with the Cer-1-P molecules tilting their acyl chains toward the water subphase. This observation is consistent with the GIXD data discussed below.

Grazing incidence x-ray diffraction

GIXD scans were recorded for all of the pressures at which the reflectivity was measured. At zero pressure, i.e., 117 Å^2/mol, no diffraction was observed for the pure water, buffer and 1 mM Ca^{2+} subphases. However, diffraction peaks were observed for the buffer + 1 mM Ca^{2+} subphase, indicating that under these conditions Cer-1-P already has a high degree of organization (data not shown).

TABLE 3 Molecular areas, bound number of water molecules, and ions (Ca^{2+} and Na$^+$) calculated from the reflectivity data, shown in Table 1

Subphase	Pure water	1 mM CaCl$_2$	Buffer	Buffer + 1 mM CaCl$_2$
A_m (Å^2)	$43.7 \pm ^{3.9}_{4.0}$	$42.2 \pm ^{4.9}_{4.7}$	$45.0 \pm ^{5.5}_{5.6}$	$43.1 \pm ^{6.7}_{5.2}$
V_{head} (Å^3)	$171 \pm ^{31}_{22}$	$171 \pm ^{31}_{22}$	$171 \pm ^{31}_{22}$	$171 \pm ^{31}_{22}$
N_{H_2O}	$5.4 \pm ^{3.8}_{5.2}$	$2.8 \pm ^{5.4}_{2.8}$	$5.2 \pm ^{4.9}_{4.8}$	$3.6 \pm ^{7.7}_{3.6}$
$N_{Ca^{2+}}$	n/a	$0.6 \pm ^{0.5}_{0.6}$	n/a	$1.1 \pm ^{0.6}_{0.5}$
N_{Na^+}	n/a	n/a	$0.3 \pm ^{0.7}_{0.3}$	n/a

Error in reflectivity and uncertainty in headgroup/tail interface taken into account.

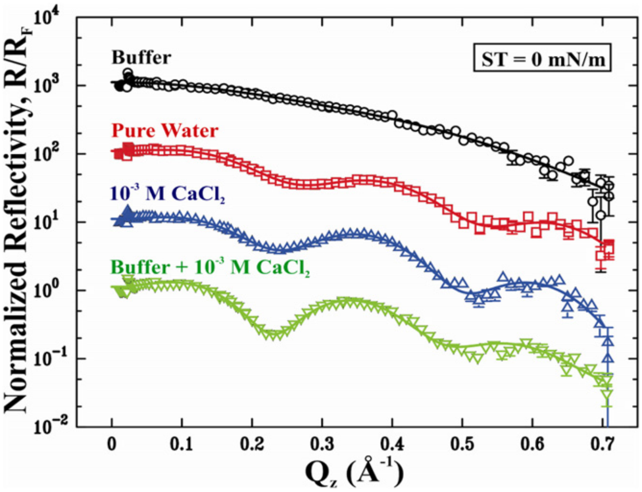

FIGURE 5 Normalized reflectivity of ceramide-1-phosphate on four different subphases as indicated at zero surface pressure. Solid lines are guides to the eye.

The intensity map of Q_z versus Q_{xy} is shown in Fig. 6, for Cer-1-P at 10 ± 1 mN/m. Cuts along Q_{xy} are shown in Fig. 7. For both the water and buffer subphase, two Bragg rods along Q_{xy} are present with indices $Q(1,1)$ and $Q(0,2)$ (using rectangular lattice spacing) respectively as shown in Fig. 6. The observation of two Bragg rods with the maximum intensity for $Q(1,1)$ shifted from $Q_z = 0$ to $Q_z > 0$ indicates a tilting of the acyl chains toward nearest neighbors (40,46,47). The same is true for Cer-1-P on 1 mM CaCl$_2$, but here the Bragg rods are very close together and for buffer + Ca^{2+} these peaks completely overlap. The fact that we observe only one peak for the buffer plus Ca^{2+} subphase, indicates an almost perfect hexagonal packing of the chains with a d-spacing of 4.16 Å and a corresponding hexagonal unit cell of area 19.99 Å^2 per chain, indicating a highly crystalline hydrocarbon chain packing (36,40,46,47). The observation that Cer-1-P is more closely packed at 10 ± 1 mN/m on buffer + 1 mM CaCl$_2$ is consistent with the observation of a weak diffraction at zero pressure. At 30 mN/m the chains of Cer-1-P are all closely packed in a hexagonal lattice for all the subphases examined with the exception of the buffer subphase where a small tilting persists to high pressure (data not shown).

The diffraction patterns observed for Cer-1-P are all indicative of either a pure hexagonal packing (one diffraction peak) of the chains or a hexagonal packing with a tilt to nearest neighbors (*NN*) (distorted hexagonal unit cell) (47). Calculation of the tilt angle is straightforward and follows from

$$\tan t = \frac{Q_z(1,1)}{\left(Q_{xy}(1,1)^2 - \left(Q_{xy}(0,2)/2\right)^2\right)^{1/2}}. \quad (5)$$

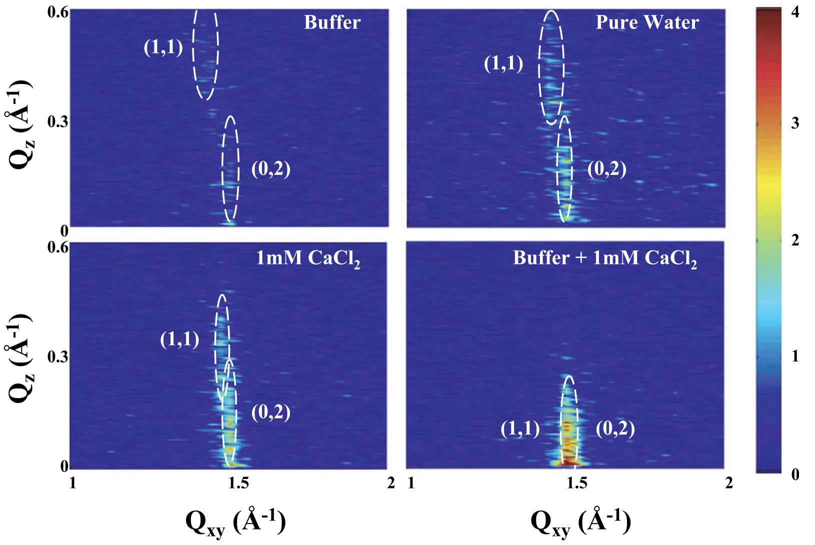

FIGURE 6 Grazing incidence x-ray diffraction maps of ceramide-1-phosphate on four different subphases as indicated at a surface pressure of 10 ± 1 mN/m. The diffraction peaks and their Q_z components are indicated in the 2D maps by a dotted ellipse.

The chain area can be calculated from the following relations,

$$Q(1,1) = \sqrt{Q_z(1,1)^2 + Q_{xy}(1,1)^2} = \sqrt{\left(\frac{2\pi}{a}\right)^2 + \left(\frac{2\pi}{b}\right)^2}, \tag{6}$$

$$Q(0,2) = Q_{xy}(0,2) = 2 \times \frac{2\pi}{b}, \tag{7}$$

where a and b are the real space lattice spacings of the rectangular unit cell enclosing one lipid molecule (i.e., two acyl chains). The peak positions $Q_z(1,1)$, and $Q_{xy}(1,1)$ and $Q_{xy}(0,2)$ shown in Table 4 are found directly from Lorentzian fits of GIXD data. The molecular area perpendicular to the tilted chains $A_1 = a \times b$, and the molecular area parallel to the subphase A_2 is found from

$$\cos t = \frac{A_1}{A_2} \tag{8}$$

The tilts and molecular areas calculated from the diffraction data using Eqs. 5–8 are listed in Table 4. The molecular areas (i.e., A_2) shown in Table 4 qualitatively agree with those found from the reflectivity data (Table 3), except that the areas found from the reflectivity are somewhat larger than those found from the GIXD. This is expected because reflectivity measurements average over small inhomogeneities due to packing defects between different crystalline regions in the monolayer, whereas the diffraction pattern is due only to the ordered regions of the monolayer.

Comparing the results of Table 4 and Figs. 6 and 7, it is clear that the main effect of Ca^{2+} is to increase the degree of crystalline packing of the acyl-chains of Cer-1-P, while strongly influencing the tilting of the acyl chains and effectively removing this tilt on the buffer subphase.

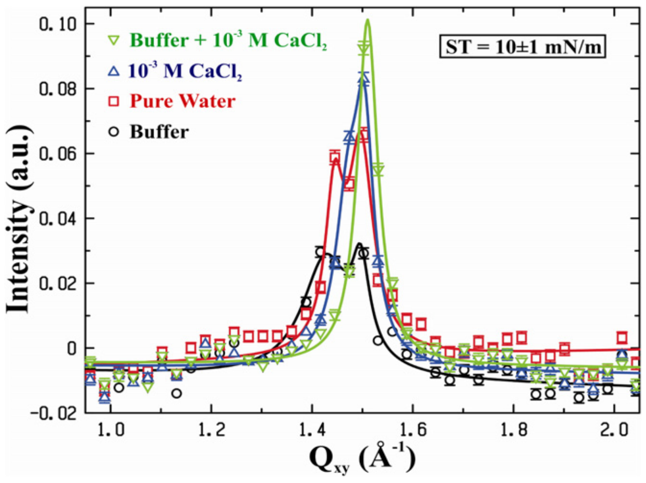

FIGURE 7 Q_{xy}-cuts of the GIXD maps of ceramide-1-phosphate from Fig. 6. Solid lines are best-fit Lorentzian curves.

DISCUSSION

In this study we investigated the phase behavior and structural properties of the minority but crucial cellular lipid ceramide-1-phosphate (Cer-1-P) at the air-liquid interface on four different water subphases. This study was aimed at evaluating the effect of the rich functionality of the Cer-1-P chemical structure (phosphomonoester, free hydroxyl group and amine linked acyl chain) on its physical properties in model membrane systems and to relate this to its potential role in biological membranes (14,15). Langmuir monolayers were chosen as an experimental model system due to their flexibility, allowing for the detailed analysis of the morphological and microscopic molecular structure of Cer-1-P without the introduction of external and potentially interfering probes (14,15,48).

Even though the overall molar concentration of Cer-1-P in biological membranes is low (22), its local molar

TABLE 4 Peak positions for GIXD data shown in Figs. 6 and 7, corresponding tilt angles (*t*), and molecular areas (A_1 and A_2) calculated from Eqs. 5–8

Subphase	Pure water	1 mM $CaCl_2$	Buffer	Buffer + 1 mM $CaCl_2$
$Q_{xy}(1,1)$ ($Å^{-1}$)	1.445 ± 0.012	1.472 ± 0.005	1.427 ± 0.012	1.510 ± 0.002
$Q_z(1,1)$ ($Å^{-1}$)	0.411 ± 0.069	0.322 ± 0.065	0.455 ± 0.071	0
$Q_{xy}(0,2)$ ($Å^{-1}$)	1.497 ± 0.005	1.504 ± 0.004	1.497 ± 0.005	1.510 ± 0.002
$Q_z(0,2)$ ($Å^{-1}$)	0	0	0	0
t (°)	18.4 ± 3.1	14.3 ± 2.8	20.5 ± 3.2	0
A_1 ($Å^2$)	40.59 ± 1.19	40.21 ± 0.78	40.65 ± 1.28	39.99 ± 0.10
A_2 ($Å^2$)	42.67 ± 0.58	41.49 ± 0.28	43.41 ± 0.59	39.99 ± 0.10
A ($Å^2$)	$43.7\pm^{3.9}_{4.0}$	$42.2\pm^{4.9}_{4.7}$	$45.0\pm^{5.5}_{5.6}$	$43.1\pm^{6.7}_{5.2}$

Areas calculated from the reflectivity data A are also shown for comparison.

concentration may be much higher. For example it is not known if Cer-1-P, like ceramide, is able to form domains and what type of interactions trigger such domain formation. It is likely that during signaling events, i.e., on the activation of Cer1p kinase, the local concentration of Cer-1-P increases (and subsequently the local concentration of ceramide decreases) to the point where local microdomains enriched in Cer-1-P may play a functional role. Such a local increase in Cer-1-P concentration will only be relevant if the enzymatic rate of Cer-1-P synthesis is higher than the rate of diffusion of Cer-1-P in the plane of the membrane. Furthermore, the intracellular pH varies among organelles of eukaryotic cells, and because Cer-1-P has a phosphomonoester headgroup, i.e., can carry two negative charges, with a pKa_2 that lies in the physiological pH range ($pKa_2 = 7.39$; 5 mol %, in a DOPC bilayer (28)) it is important to compare the monolayer behavior of Cer-1-P on substrates with a different pH. Additionally, the local Ca^{2+} concentration varies in a cell and at least some physiological functions of Cer-1-P may be modulated by increases in Ca^{2+} concentration (13,18,19,21). In light of this, we determined the molecular structure of pure Cer-1-P monolayers on a pure water subphase with a pH of ~6.0 that is well within the low acidic range ($5.5 < pH < 6.5$) generally attributed to pure water in air, and a pH 7.2 buffered subphase with and without 1 mM $CaCl_2$.

Molecular structure of Cer-1-P on water and buffer subphases

The isotherms shown in Fig. 2 all indicate that Cer-1-P forms highly condensed monolayers on all the subphases investigated in this study. This is further supported by the BAM and x-ray experiments. Note that the monolayer area represented by the isotherms shown in Fig. 2 *A* are only approximate in that significant (5–10%) area differences occur between isotherms. BAM clearly shows multiple "crystalline" domains for Cer-1-P on water right after spreading and a breaking and collapse mechanism after and on compression that is indicative of a 2D crystalline layer. Cer-1-P on buffer appears to be considerably more uniform. The dark regions in Fig. 3 arise from a clean water surface or a coexisting 2D gas phase (dilute noninteracting molecules). The collapse and breaking behavior of the monolayer on buffer is also very distinct from that on water in that no clear 3D collapse structures are observed (as evidenced by BAM) and that cracks in the monolayer tend to spontaneously fuse reversibly. Interestingly, this self-healing property of Cer-1-P on buffer is more reminiscent of the self-healing properties of fluid lipid bilayers (7).

X-ray reflectivity measured right after spreading supports the conclusion that Cer-1-P on buffer differs significantly from the corresponding monolayers on the other investigated subphases. Combined with the BAM data this suggests that the Cer-1-P monolayer is considerably thinner and/or more uniform on buffer right after spreading, i.e., on buffer no fringes are observed over the entire Q_z region probed, suggestive of a 2D gas-like structure. The thinner, more uniform, layer on buffer right after spreading is most likely caused by a chain tilting of Cer-1-P toward the aqueous subphase. Indeed, GIXD data confirms that at higher pressures the Cer-1-P molecules are more tilted on the buffer subphase than on any of the other subphases investigated (Table 4).

The difference in behavior of Cer-1-P on water and buffer can be qualitatively understood as follows. On water, pH of ~6.0, Cer-1-P in our monolayers likely carries only one negative charge as indicated by the pKa_2 of ~7.4 (28). Here, Cer-1-P is able to form a tight intermolecular hydrogen bond network linking the individual phosphomonoesters together. This H-bond network is complementary to the hydrogen bonds that can be formed between the free hydroxyl group and amine group in the backbone structure of this lipid, which is schematically shown in Fig. 8 *A*. Based on the electronegativity of the individual groups, these are the most plausible H-bonds that can be formed between Cer-1-P molecules, but clearly our data do not provide direct experimental evidence for the existence of such bonds. The propensity to form multiple hydrogen bonds between individual Cer-1-P molecules in this pH range is the likely cause for the crystalline 2D behavior on water, and the large Gibbs elasticity inferred from the slope of the π/A-isotherms. It also explains why Cer-1-P on water, after compression and decompression does not respread. Hydrogen bonds formed between the individual phosphate groups of adjacent molecules may also explain the higher collapse pressure of Cer-1-P compared to ceramide (5,29). This behavior is

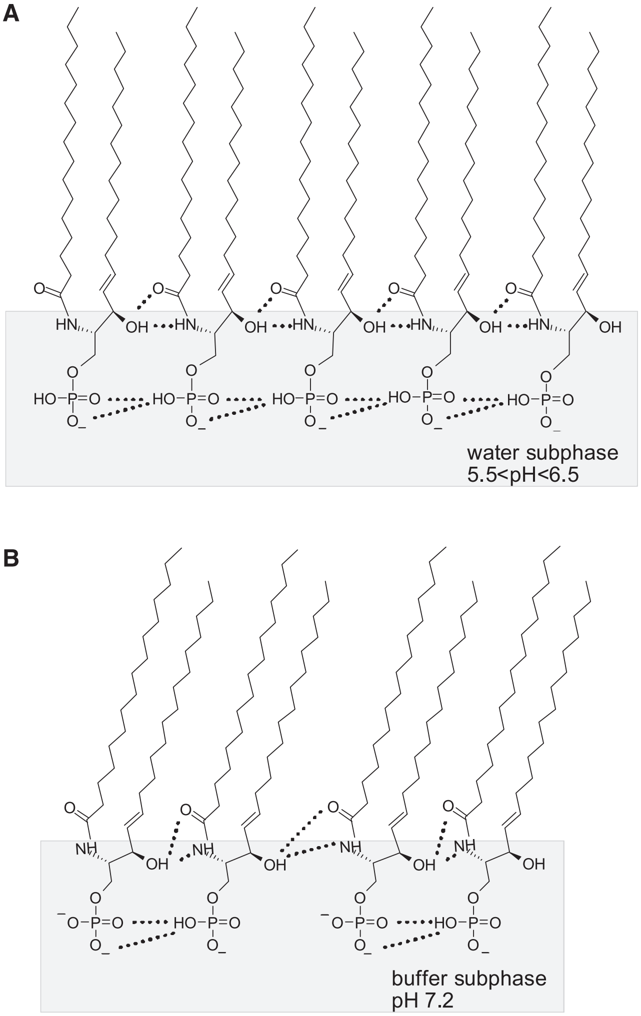

FIGURE 8 Schematic molecular model of ceramide-1-phosphate in monomolecular layers at the air/water (*A*) and air/buffer (*B*) interface at high pressures. Orientation and organization of the individual molecules is based on the reflectivity and GIXD measurements at 10 and 30 mN/m. Dotted lines in the figure indicate potential hydrogen bonds. The water (buffer) interface is indicated for illustration purposes only and is not a sharp interface in reality.

similar to that observed for phosphatidic acid, which also shows an enhanced stabilization of lipid monolayers and bilayers between the pKa_1 and pKa_2 (49–51).

On buffer at pH 7.2 the situation is considerably different. Here the overall charge of Cer-1-P is higher than -1 and (assuming a pKa_2 of 7.4 (28)) nearly half of the Cer-1-P carries a negative charge of 2. This higher negative charge would result in a less tight hydrogen bond network between the phosphate groups, a larger effective molecular area, and subsequently a potential for the acyl-chains to tilt away from the surface normal, thus increasing the chain-chain interaction, as shown schematically in Fig. 8 *B*. After spreading at high molecular areas and subsequent compression, the surface charge density increases, effectively decreasing the negative charge of Cer-1-P consistent with the Gouy-Chapman theory. Thus at high pressures Cer-1-P is able to form a solid like monolayer on the buffer subphase as indicated by the high values of E_G. However, on decompression the effective surface charge density decreases again, increasing the effective negative charge of Cer-1-P, thereby facilitating the spreading of Cer-1-P on the buffer subphase.

The effect of calcium in the subphase on the monolayer properties is striking and seems to be at least twofold. First, Ca^{2+} ions will bind to Cer-1-P and effectively screen the negative charge of the phosphomonoester headgroup, resulting in a smaller molecular area. Second, Ca^{2+} ions dehydrate the headgroup of Cer-1-P and clearly decrease the tilting of the acyl-chains of Cer-1-P. Third, Ca^{2+} might bridge neighboring Cer-1-P molecules. The data clearly show differences between the effect of calcium present in water versus in buffer subphases. In the case of the water subphase, the addition of 1 mM Ca^{2+} at 10 mN/m decreases the tilting of the hydrocarbon chains by only ~4°, whereas addition of the same amount of Ca^{2+} to the buffer subphase decreases the tilting by ~20°. This effect is most likely caused by the larger accumulation of Ca^{2+} in the electric double layer near the phosphomonoester headgroup of Cer-1-P in the case of the buffer subphase. This is evident from the calculated number of calcium ions bound to the headgroup. The larger interaction of Ca^{2+} with the headgroup of Cer-1-P is caused by the overall larger degree of ionization (degree of negative charge) of the headgroup of Cer-1-P on the buffer compared to the water subphase (see reference (28) for titration curves). Note that although Ca^{2+} dramatically affects the tilt of the hydrocarbon chains of Cer-1-P at low pressure, this is not reflected in the rigidity of the layers. This seemingly paradoxical set of behaviors may be understood by the following argument: Cer-1-P is unique in that its chemical structure contains a phosphomonoester headgroup, a sphingoid base and acyl chain attached via an amine bond. This structure allows for multiple intermolecular hydrogen bonds between individual phosphates, and sphingoid backbones, which seem to dominate the rigidity of the layers. Our data indicates that under these circumstances tilting of the chains does not have a large effect on the rigidity.

Fig. 8, *A* and *B*, shows a working model for Cer-1-P in a monolayer on a pure water and buffer subphase at high pressure. The model illustrates the proposed hydrogen bonds formed between the phosphate headgroups and backbone hydroxyl and amine groups. The structure on buffer differs from that on water in such a way that the headgroups carry on average more negative charge decreasing the degree of H-bond formation, resulting in a tilting of the acyl-chains away from the surface normal.

Comparison with previous data and biological implications

Our observations clearly set Cer-1-P apart from the more common sphingolipids, ceramide, and sphingomyelin.

Both Cer and SM were found to form highly condensed monolayers similar to those of Cer-1-P (5,6,29). However, the hydrocarbon-chains of Cer-1-P are found to tilt away from the surface normal (even at high surface pressure) and no corrugation of the acyl-chains is observed, i.e., the electron density of the chain region can be completely and adequately described by a single slab of electron density unlike that of ceramide and sphingomyelin (5,6). Tilting of the hydrocarbon-chains of Cer-1-P on pH 7.2 buffer is consistent with the behavior of egg ceramide derived Cer-1-P in bilayers in the sub gel/crystalline phase at identical conditions of pH and salt concentration (28).

The results discussed in this study suggest a large effect of the phosphomonoester headgroup of Cer-1-P on its biological functions. For example, it is currently still unclear how this phosphomonoester will effect formation of ordered domains with other sphingo- and/or glycero-(phospho-) lipids. Our data suggest that the potential to form domains will critically depend on intracellular pH and the presence of divalent cations.

Interactions with Ca^{2+} are clearly important from the point of view of lipid/protein interaction. Most relevant in this regard is the interaction of Cer-1-P with group IVA $cPLA_2\alpha$ ($cPLA_2\alpha$). Previous studies by Chalfant et al. (18,19,52) showed the need for Cer-1-P for membrane translocation and binding of this enzyme. In in vitro studies it was shown that Cer-1-P binds to the C2-domain of $cPLA_2\alpha$ and mutants lacking one or more of the three basic amino acids (Arg^{57}, Lys^{58}, Arg^{58}) in a β-grove of this domain greatly inhibit binding to Cer-1-P (52). Furthermore, it was shown that $cPLA_2\alpha$ binding was Ca^{2+} dependent, but that Ca^{2+} concentrations $>300\ \mu M$ actually inhibited Cer-1-P binding. These seemingly contradictory results may be rationalized based on our results and data published recently on phosphatidylserine.

In this study, we showed that 1 mM Ca^{2+} in the subphase clearly neutralizes any negative charge present in the Cer-1-P headgroup/water interface, i.e., Ca^{2+} has a strong affinity for the phosphomonoester of Cer-1-P. This strong interaction persists in even a 100-fold larger Na^+ concentration as used in the buffer experiments. The binding of Ca^{2+} to the phosphomonoester headgroup of Cer-1-P not only results in a screening of the negative charge of the phosphomonoester, but also results in an increase in the negative charge as predicted by the Gouy-Chapman-Stern theory. This was experimentally shown for phosphatidic acid, which carries an identical phosphomonoester headgroup (53), and thus shows similar ionization behavior considering differences in the chemical structures of the molecules (i.e., Cer-1-P and PA). Our results are also consistent with previous findings for phosphatidic acid where it was shown that Ca^{2+} is able to neutralize the negative charge even at smaller (sub mM) concentrations (43,44).

Recent work on phosphatidylserine supports the role of Ca^{2+} in peripheral membrane protein binding to a receptor membrane (54). Phosphatidylserine together with a smaller amount of phosphatidylinositol provides for most of the negative charge (~30%) found on the cytosolic leaflet of the plasmalemma (55,56). Grinstein and co-workers (54) have shown that when the negative surface charge of this membrane is decreased on Ca^{2+} fluxes, strongly cationic proteins relocalize to endocytic compartments, underscoring the control imparted by Ca^{2+} in peripheral membrane protein location.

In the case of Cer-1-P binding to $cPLA_2\alpha$ it is likely that Ca^{2+} is required only for the proper folding of the C2 domain. At higher Ca^{2+} concentrations Ca^{2+} also binds to the Cer-1-P in the membrane, thereby effectively abolishing the electrostatic interaction required for the initial electrostatic interaction between $cPLA_2\alpha$ and Cer-1-P.

SUPPORTING MATERIAL

Further discussion, two movies, and two figures are available at http://www.biophysj.org/biophysj/supplemental/S0006-3495(09)00317-8.

The authors thank Duane Redfern, and Katrice King for practical discussions and Douglas Robinson of Iowa State and APS for his help with the synchrotron x-ray experiments.

This work was supported, in part, by the U.S. National Science Foundation grants DMR-0637221 and CHE-0724082, and a Research Challenge award from the Ohio Board of Regents. Use of the Advanced Photon Source (APS) was supported by the U.S. Department of Energy, Basic Energy Sciences, Office of Science (contract No. W-31-109-Eng-38). The Midwest Universities Collaborative Access Team sector at the APS is supported by the U.S. Department of Energy, Basic Energy Sciences, Office of Science. The work at Ames Laboratory was supported by the U.S. Department of Energy, Basic Energy Sciences, Office of Science (contract No. DE-AC02-07CH11358).

Any opinions, findings, and conclusions or recommendations expressed in this publication are those of the authors and do not necessarily reflect the views of the National Science Foundation.

REFERENCES

1. Spiegel, S., and A. H. Merrill, Jr. 1996. Sphingolipid metabolism and cell growth regulation. *FASEB J.* 10:1388–1397.
2. Huitema, K., J. van den Dikkenberg, J. F. Brouwers, and J. C. Holthuis. 2004. Identification of a family of animal sphingomyelin synthases. *EMBO J.* 23:33–44.
3. Tafesse, F. G., P. Ternes, and J. C. Holthuis. 2006. The multigenic sphingomyelin synthase family. *J. Biol. Chem.* 281:29421–29425.
4. Vaknin, D. 2003. Structure-function relations in self-assembled C18- and C20-Sphingosines monolayers at gas/water interfaces. *J. Am. Chem. Soc.* 125:1313–1318.
5. Vaknin, D., and M. S. Kelley. 2000. The structure of D-erythro-C18 ceramide at the air-water interface. *Biophys. J.* 79:2616–2623.
6. Vaknin, D., M. S. Kelley, and B. M. Ocko. 2001. Sphingomyelin at the air-water interface. *J. Chem. Phys.* 115:7697–7704.
7. Mouritsen, O. G. 2005. Life—As a Matter of Fat: The Emerging Science of Lipidomics. Springer-Verlag, Berlin.
8. Engstrom, S., K. Ekelund, J. Engblom, L. Eriksson, E. Sparr, et al. 2000. The skin barrier from a lipid perspective. *Acta Derm. Venereol.* 208:31–35.
9. Silva, C. L., D. Topgaard, V. Kocherbitov, J. J. Sousa, A. A. Pais, et al. 2007. Stratum corneum hydration: phase transformations and mobility

in stratum corneum, extracted lipids and isolated corneocytes. *Biochim. Biophys. Acta*. 1768:2647–2659.

10. Simons, K., and E. Ikonen. 1997. Functional rafts in cell membranes. *Nature*. 387:569–572.
11. Castro, B. M., R. F. de Almeida, L. C. Silva, A. Fedorov, and M. Prieto. 2007. Formation of ceramide/sphingomyelin gel domains in the presence of an unsaturated phospholipid: a quantitative multiprobe approach. *Biophys. J*. 93:1639–1650.
12. Silva, L. C., R. F. de Almeida, B. M. Castro, A. Fedorov, and M. Prieto. 2007. Ceramide-domain formation and collapse in lipid rafts: membrane reorganization by an apoptotic lipid. *Biophys. J*. 92:502–516.
13. Gomez-Munoz, A. 2004. Ceramide-1-phosphate: a novel regulator of cell activation. *FEBS Lett*. 562:5–10.
14. Demel, R. A. 1994. Monomolecular layers in the study of biomembranes. *Subcell. Biochem*. 23:83–120.
15. Brockman, H. 1999. Lipid monolayers: why use half a membrane to characterize protein-membrane interactions? *Curr. Opin. Struct. Biol*. 9:438–443.
16. Hinkovska-Galcheva, V., L. A. Boxer, A. Kindzelskii, M. Hiraoka, A. Abe, et al. 2005. Ceramide 1-phosphate, a mediator of phagocytosis. *J. Biol. Chem*. 280:26612–26621.
17. Swartz, K. J. 2006. Greasing the gears of potassium channels. *Nat. Chem. Biol*. 2:401–402.
18. Pettus, B. J., A. Bielawska, S. Spiegel, P. Roddy, Y. A. Hannun, et al. 2003. Ceramide kinase mediates cytokine- and calcium ionophore-induced arachidonic acid release. *J. Biol. Chem*. 278:38206–38213.
19. Pettus, B. J., A. Bielawska, P. Subramanian, D. S. Wijesinghe, M. Maceyka, et al. 2004. Ceramide 1-phosphate is a direct activator of cytosolic phospholipase A2. *J. Biol. Chem*. 279:11320–11326.
20. Pettus, B. J., C. E. Chalfant, and Y. A. Hannun. 2004. Sphingolipids in inflammation: roles and implications. *Curr. Mol. Med*. 4:405–418.
21. Nakamura, H., T. Hirabayashi, M. Shimizu, and T. Murayama. 2006. Ceramide-1-phosphate activates cytosolic phospholipase A2alpha directly and by PKC pathway. *Biochem. Pharmacol*. 71:850–857.
22. Dressler, K. A., and R. N. Kolesnick. 1990. Ceramide 1-phosphate, a novel phospholipid in human leukemia (HL-60) cells. Synthesis via ceramide from sphingomyelin. *J. Biol. Chem*. 265:14917–14921.
23. Gomez-Munoz, A., J. Y. Kong, K. Parhar, S. W. Wang, P. Gangoiti, et al. 2005. Ceramide-1-phosphate promotes cell survival through activation of the phosphatidylinositol 3-kinase/protein kinase B pathway. *FEBS Lett*. 579:3744–3750.
24. Gomez-Munoz, A., J. Y. Kong, B. Salh, and U. P. Steinbrecher. 2004. Ceramide-1-phosphate blocks apoptosis through inhibition of acid sphingomyelinase in macrophages. *J. Lipid Res*. 45:99–105.
25. Subramanian, P., R. V. Stahelin, Z. Szulc, A. Bielawska, W. Cho, et al. 2005. Ceramide 1-phosphate acts as a positive allosteric activator of group IVA cytosolic phospholipase A2 alpha and enhances the interaction of the enzyme with phosphatidylcholine. *J. Biol. Chem*. 280:17601–17607.
26. van Blitterswijk, W. J., A. H. van der Luit, R. J. Veldman, M. Verheij, and J. Borst. 2003. Ceramide: second messenger or modulator of membrane structure and dynamics? *Biochem. J*. 369:199–211.
27. Goni, F. M., and A. Alonso. 2006. Biophysics of sphingolipids I. Membrane properties of sphingosine, ceramides and other simple sphingolipids. *Biochim. Biophys. Acta*. 1758:1902–1921.
28. Kooijman, E. E., J. Sot, L. R. Montes, A. Alonso, A. Gericke, et al. 2008. Membrane organization and ionization behavior of the minor but crucial lipid ceramide-1-phosphate. *Biophys. J*. 94:4320–4330.
29. Loffgren, H., and I. Pascher. 1977. Molecular arrangements of sphingolipids. The monolayer behavior of ceramides. *Chem. Phys. Lipids*. 20:273–284.
30. Ekelund, K., L. Eriksson, and E. Sparr. 2000. Rectangular solid domains in ceramide-cholesterol monolayers - 2D crystals. *Biochim. Biophys. Acta*. 1464:1–6.
31. Sparr, E., L. Eriksson, J. A. Bouwstra, and K. Ekelund. 2001. AFM study of lipid monolayers: III. Phase behavior of ceramides, cholesterol and fatty acids. *Langmuir*. 17:164–172.
32. Rouser, G., S. Fkeischer, and A. Yamamoto. 1970. Two dimensional thin layer chromatographic separation of polar lipids and determination of phospholipids by phosphorus analysis of spots. *Lipids*. 5:494–496.
33. Henon, S., and J. Meunier. 1991. Microscope at the Brewster-angle—direct observation of 1st-order phase-transitions in monolayers. *Rev. Sci. Instrum*. 62:936–939.
34. Honig, D., and D. Mobius. 1991. Direct visualization of monolayers at the air-water-interface by Brewster-angle microscopy. *J. Phys. Chem*. 95:4590–4592.
35. Vaknin, D. 2003. X-ray diffraction techniques for liquid surfaces and monomolecular layers. *Characterization of Materials*. 2:1027–1047.
36. Als-Nielsen, J., and K. Kjaer. 1989. *In* Phase Transitions in Soft Condensed Matter. T. Riste and D. Sherrington, editors. Plenum, New York.
37. Parrat, L. G. 1954. Phys. Rev. 59:359.
38. Born, M., and E. Wolf. 1959. Principles of Optics. McMillan, New York.
39. Bu, W., D. Vaknin, and A. Travesset. 2006. How accurate is Poisson-Boltzmann theory for monovalent ions near highly charged interfaces? *Langmuir*. 22:5673–5681.
40. Kjaer, K. 1994. Some simple ideas on x-ray reflection and grazing-incidence diffraction from thin surfactant films. *Physica B (Amsterdam)*. 198:100.
41. http://environmentalchemistry.com/yogi/periodic/ionicradius.html.
42. Cevc, G. 1990. Membrane electrostatics. *Biochim. Biophys. Acta*. 1031:311–382.
43. Travesset, A., and D. Vaknin. 2006. Bjerrum pairing correlations at charged interfaces. *Europhys. Lett*. 74:181–187.
44. Faraudo, J., and A. Travesset. 2007. Phosphatidic acid domains in membranes: effect of divalent counterions. *Biophys. J*. 92:2806–2818.
45. Nagle, J. F., and S. Tristram-Nagle. 2000. Structure of lipid bilayers. *Biochim. Biophys. Acta*. 1469:159–195.
46. Als-Nielsen, J., D. Jacquemain, K. Kjaer, F. Leveiller, M. Lahav, et al. 1994. Principles and applications of grazing incidence x-ray and neutron scattering from ordered molecular monolayers at the air-water interface. *Phys. Rep*. 246:251–313.
47. Kaganer, V. M., H. Mohwald, and P. Dutta. 1999. Structure and phase transitions in Langmuir monolayers. *Rev. Mod. Phys*. 71:779–819.
48. Gaines, G. L. J. 1966. Insoluble Monolayers at Liquid-Gas Interfaces. Intersciences Publishers, New York.
49. Trauble, H., and H. Eibl. 1974. Electrostatic effects on lipid phase transitions: membrane structure and ionic environment. *Proc. Natl. Acad. Sci. USA*. 71:214–219.
50. Eibl, H., and A. Blume. 1979. The influence of charge on phosphatidic acid bilayer membranes. *Biochim. Biophys. Acta*. 553:476–488.
51. Jahnig, F., K. Harlos, H. Vogel, and H. Eibl. 1979. Electrostatic interactions at charged lipid membranes. Electrostatically induced tilt. *Biochemistry*. 18:1459–1468.
52. Stahelin, R. V., P. Subramanian, M. Vora, W. Cho, and C. E. Chalfant. 2007. Ceramide-1-phosphate binds group IVA cytosolic phospholipase a2 via a novel site in the C2 domain. *J. Biol. Chem*. 282:20467–20474.
53. Kooijman, E. E., K. M. Carter, E. G. van Laar, V. Chupin, K. N. Burger, et al. 2005. What makes the bioactive lipids phosphatidic acid and lysophosphatidic acid so special? *Biochemistry*. 44:17007–17015.
54. Yeung, T., G. E. Gilbert, J. Shi, J. Silvius, A. Kapus, et al. 2008. Membrane phosphatidylserine regulates surface charge and protein localization. *Science*. 319:210–213.
55. Op den Kamp, J. A. 1979. Lipid asymmetry in membranes. *Annu. Rev. Biochem*. 48:47–71.
56. van Meer, G. 1998. Lipids of the Golgi membrane. *Trends Cell Biol*. 8:29–33.